AIChE

Molecular Transport in Nanopores with Broad Pore-Size Distribution

Fu Yang Wang, Zhong Hua Zhu, and Victor Rudolph
Division of Chemical Engineering, School of Engineering, The University of Queensland, Brisbane, Qld. 4072, Australia

DOI 10.1002/aic.11520
Published online June 13, 2008 in Wiley InterScience (www.interscience.wiley.com).

A methodology is developed for molecular transport in nanopores, based on physical attributes requiring neither molecular dynamics simulations nor empirical correlations. The proposed approach is reasonably rigorous yet easy to apply. The models extend the conventional theoretical framework[1–3] by eliminating key restrictive assumptions, such as uniform pore-size and hard-sphere molecules using several new mathematical treatments and the multisite potential equation,[4,5] making them more applicable to practical porous media. Importantly, one of the models reported using integral mean value theory develops an equation with the same format as a widely used formula with two empirical parameters, providing new physical insights into the utility of this model. Literature data for carbon tetrachloride and benzene transport in a commercial Ajax activated carbon are used as two case studies to demonstrate the applicability of the proposed methodology to practical systems, with good agreement between simulations and measurement data. © 2008 American Institute of Chemical Engineers *AIChE J,* 54: 2009–2023, 2008
Keywords: adsorption, complex fluids, diffusion, mathematical modeling, porous media

Introduction

Molecular transport in porous media consists of viscous flow, molecular, and Knudsen diffusion in macro- and mesopores, as well as adsorbed-phase diffusion (surface diffusion) in micropores. Among these processes, surface diffusion remains the least understood, and is the main focus of this study. The ranges of the slit-pore widths for micro-, meso- and macropores are defined as[6] 5–20 Å, 20–500 Å and $>$ 500 Å, respectively. This article focuses on molecule transport in micropores and small-size mesopores (20–100 Å), which we collectively call nanopores.

The research methodologies for surface diffusion can be broadly classified into two categories: an engineering approach using empirical parameters obtained from experimental measurements,[7–9] and a fundamental approach based on molecular simulations, but which can currently be applied only for idealized systems.[1–3,10] There are advantages and disadvantages for both approaches. The engineering approach provides useful descriptions for industrial applications, but largely sacrifices physical insights and requires extensive experimental extraction of the empirical parameters, which are not generally transferrable to new situations. The fundamental approach on the other hand, rigorously computes physical values from first principles, but this requires significant idealization, very restrictive mathematical assumptions and long computing times. An intermediate approach, requiring neither empirically fitted parameters nor reliance on time-consuming molecular dynamics simulations with very restrictive idealizations, represents the objective of this work. Although certain approximations are necessary in the development of an intermediate model, they are reasonably rigorous and suitable for most industrial applications. The main characteristics of the proposed modeling methodology, together with the limitations of the current methods that this article seeks to address are summarized as follows:

1. Fundamental studies using molecular dynamics simulations require well defined, generally highly idealized systems with prespecified uniform pore widths and computational complexity, which are impractical for most industrial operations involving porous media. This article develops computationally simpler models for molecule transport in

Correspondence concerning this article should be addressed to F. Y. Wang at f.wang@eng.uq.edu.au.

micro-/mesopores and permits broad pore-size distributions, through an extension of the methods reported by Bhatia and Nicholson[1,2] and Jepps et al.[3]

2. In conventional practical and fundamental approaches, the molecules are assumed to be regular hard spheres to allow the application of the well-known Lennard-Jones[11] and Steele[12] potential equations. This assumption is eliminated here, through the incorporation of a multisite potential developed by Do and Do[4,5] into our models.

3. The "practical" approaches that have been reported, e.g., Bae and Do,[7,8] normally consist of a number of empirical parameters that need to be evaluated using experimental data. Since it is very difficult to measure the surface diffusion flux directly, the physical meaning of these parameters remains obscure. For example, in the absence of better information, we have used self-diffusivity to estimate surface diffusivity,[9] but without sound scientific justification. Furthermore, there remains some divergence between fundamental studies and industrial applications, evidenced by the lack of experimental validations of the fundamental results. We seek here to fill, at least in part, the identified incompatibilities through theoretical derivation, numerical simulation and experimental verification.

4. Fundamental, often mathematically complex theoretical representations need to be cast into formulations that are easy to understand and simple to use, if they are to be widely adopted. This principle is applied here through e.g., the application of integral mean value theory to simplify integral representations and computations; development of a simple (although approximate) equation to relate the molecule density with potential energy; and casting fundamental equations into the same format as the familiar empirical models. This serves also to reveal the underlying meaning of the empirical fitting parameters.

5. A commonly used approximation is averaging parameters over the micropore size, a practice which can result in misleading outcomes. A quantitative analysis is provided to demonstrate the error and discourage this incorrect practice.

The methods proposed here and their advantages are illustrated through two examples, relating to carbon tetrachloride and benzene transport through Ajax activated carbon.

Multiple Site Potential Energy Models

The study of molecular transport in nanopores requires computation of potential energies between molecules in the fluid phase and atoms in the solid phase. The commonly accepted single-site Lennard-Jones[11] 12-6 and Steele[12] 10-4-3 potential energy equations work well for small molecules. However, for large molecules, such as carbon tetrachloride (CCl_4) and benzene (C_6H_6), conventional single-site potential energy models developed by assuming interactions between regular hard spheres lead to significant errors due to violation of the underlying assumptions. Consequently, multisite potential energy models should be used for systems consisting of large molecules.[4,5] In this article, we use CCl_4 and C_6H_6 in slit graphite pores as two example systems, based on multisite potential energy models, to develop the modeling methodology for the rigorous study of molecular transport in nanopores with broad pore-size distribution.

The CCl_4 system is described in some detail followed by a briefer explanation of the C_6H_6 system, since this follows a similar modeling strategy. Three configurations of CCl_4 in a slit-shaped graphite pore, namely tripod, invert tripod, and 2 rad configurations, are shown in the top section of Figure 1. Based on molecular dynamics simulations, Do and Do[4] have made the following observations: (1) Most particles have the tripod configuration, which is the most energetically favored orientation; (2) A small number of particles have the inverted tripod configuration, which is entropically favorable, but not energetically optimal; and (3) An intermediate number of particles adopt the configuration with an angle of 120° (2 rad), which balances the entropic and enthalpic driving factors. Since the majority of particles adopt the tripod configuration, it is used here in the computation of potential energies. Although only the tripod configuration is used in the simulations under the particular operational conditions, two other orientations can be readily incorporated in the model under other conditions if appropriate. The proportions of various configurations, obtained through molecular dynamics simulations, are provided by Do and Do.[4]

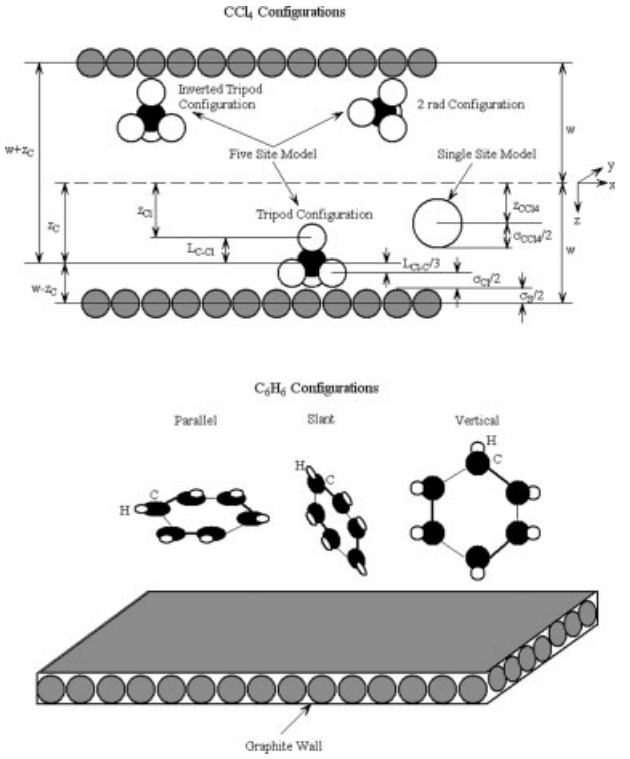

Figure 1. Configurations of CCl_4 and C_6H_6 in slit-shaped graphite pores.

There are also three orientations for C_6H_6 in slit-shaped graphite pores, namely parallel, slant and vertical orientations[5] as shown in the bottom section of Figure 1. Do and Do[5] observed, on the basis of molecular dynamic simulations, that at very low-loading, most benzene molecules take the parallel orientation which represents the most favorably energetic position. When the benzene loading is increased, but still retaining submonolayer coverage, some benzene molecules will adopt slant configurations due to the quadrupolar interactions among the benzene molecules, although most remain horizontal along the pore walls. Since we are working on systems under low-pressures ($P < 800$ Pa), the

vast majority of molecules adopt the parallel orientation as quantified by Do and Do.[5] Consequently, only the parallel orientation is used in our computations for simplicity. As with the CCl_4 system, if other molecular orientations become significant, e.g., with increased pressures, a linear combination method easily addresses multiconfiguration systems, without computational difficulties.

The multisite, Steele 10-4-3 potential energy equation for slit-shaped pores is given by[12]

$$\Phi_i(z_i,w)=\frac{5}{3}\Phi_{i0}\left\{\frac{2}{5}\left[\frac{\sigma_{is}^{10}}{(w+z_i)^{10}}+\frac{\sigma_{is}^{10}}{(w-z_i)^{10}}\right]-\left[\frac{\sigma_{is}^{4}}{(w+z_i)^{4}}+\frac{\sigma_{is}^{4}}{(w+z_i)^{4}}\right]-\left[\frac{\sigma_{is}^{4}}{3\Delta(0.61\Delta+w+z)^{3}}+\frac{\sigma_{is}^{4}}{3\Delta(0.61\Delta+w-z_i)^{3}}\right]\right\}$$

$$\Phi_{i0}=\frac{6}{5}\pi\rho_s\varepsilon_{is}\sigma_{is}^2\Delta;\ i=1,\ldots,n_c \quad (1)$$

In Eq. 1, z_i is the distance between the atom i of the fluid molecule and the central plane of the pore, w is the half width of slit-shaped pores, Φ_{i0} is the minimum interaction energy between the atom i of the fluid molecule and a single lattice layer of the adsorbent, ρ_s is the number of lattice atoms per unit volume, Δ is the spacing of lattice layers, ε_{is} and σ_{is} are the cross potential well depth, and the effective diameter for the i^{th} atom of the adsorbate molecule and the adsorbent atom, and n_c is the total number of atoms in a fluid molecule. The cross parameters are calculated using the Lorentz-Berthelot rules[11] as follows: $\varepsilon_{is}=(\varepsilon_i\varepsilon_s)^{1/2}$, and $\sigma_{is}=(\sigma_i+\sigma_s)/2$. The pairs ($\varepsilon_s$, σ_s) and (ε_i, σ_i) are the Lennard-Jones parameters for a surface atom and the i^{th} atom of fluid molecule, respectively. It should be noted that the Steele 10-4-3 potential energy equation described by Eq. 1 is an approximation. This factor may be more significant for the diffusion inside the small pores, as reviewed by Rao et al.[13] In order to minimize errors induced by the approximation, the solid-fluid interaction energy is usually adjusted with the introduction of a solid-fluid binary interaction parameter, k_{sf} such that the experimental Henry's constant is reproduced by the molecular dynamic simulations[4,5], that is

$$\varepsilon_{is}=\left(1-k_{sf}\right)\sqrt{\varepsilon_i\varepsilon_s} \quad (2)$$

It has been shown by Do and Do[4,5] that satisfactory results can be obtained by adjusting k_{sf} between -0.05 to 0 for CCl_4 and C_6H_6. For the computation of the interaction potential energy between atom i of the fluid molecule, and the homogeneous flat solid substrate, Eq. 1 is reduced to

$$\Phi_i(z_{is},w)=\left\{\frac{5}{3}\Phi_{i0}\left\{\frac{2}{5}\left(\frac{\sigma_{is}}{z_{is}}\right)^{10}-\left(\frac{\sigma_{is}}{z_{is}}\right)^{4}-\frac{\sigma_{is}^4}{3\Delta(0.61\Delta+z_{is})^3}\right\}\right.\quad i=1,\ldots,n_c \quad (3)$$

where z_{is} is the center to center distance between the i^{th} fluid atom and the solid atom. Consequently, the solid-fluid interaction is

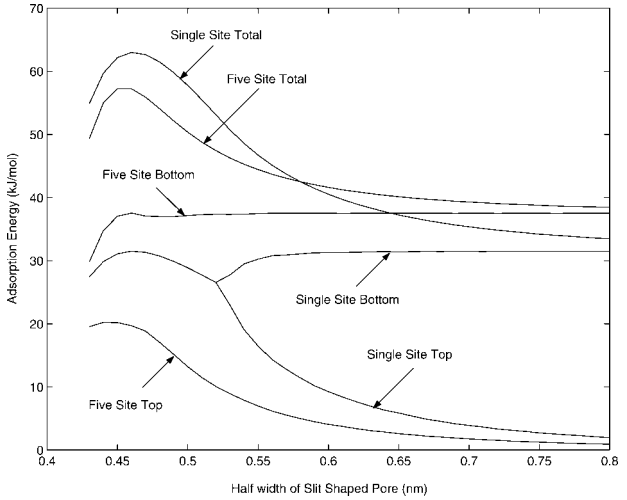

Figure 2. CCl_4 adsorption energy profiles predicted by single- and five-site models.

$$\Phi=\sum_{i=1}^{n_c}\Phi_i \quad (4)$$

The relative positions of the C atom, and four Cl atoms in a CCl_4 molecule can be determined using the relationships shown in Figure 1. The numerical values used in the simulations are summarized as follows: $L_{C\text{-}Cl}$ = 1.766 Å, σ_{Cl} = 3.50 Å, σ_C = 4.60 Å, σ_s = 3.40 Å, σ_{CCl4} = 5.95 Å.

The total adsorption energy profiles for both the single-site and five-site models are shown in Figure 2, together with the bottom and top surface contributions. The adsorption energy is defined as the negative minimum value of the energy well. There are significant differences between the models, as Figure 2 identifies. In the small pore-size range, the single-site model overpredicts the adsorption energy, whereas it underpredicts in large pores, leading to a crossover of the two curves. An analysis of the fluid-solid interactions for different configurations provides the explanation. The contributions from both surfaces in slit-shaped pores to adsorption energies using single-site and five-site models are also depicted in Figure 2.

It can be seen from Figure 2 that for $w < 5.2$ Å, the contributions to the adsorption energy from both surfaces are identical as predicted by the single-site model, due to the assumption of geometrical symmetry of the molecules. In contrast, the five-site model predicts a large difference between the contributions from the surfaces (in the small pore-size range) due to the asymmetry of CCl_4 molecules. The reduction of adsorption energy with pore-size results from the reduced attractive force from the opposite surface. In large pores, the five-site model predicts higher adsorption energy than the single-site model, because most CCl_4 molecules adopt the tripod configuration, which is more energetically advantageous than the regular sphere configuration. However, in small pores, a tripod configuration with respect to one surface becomes invert tripod configuration with respect to the opposite surface, providing less overall attraction compared with a sphere. Since the multisite model more accurately represents reality, with clearer physical insights than the hard-sphere concept,[4] it is used in this study.

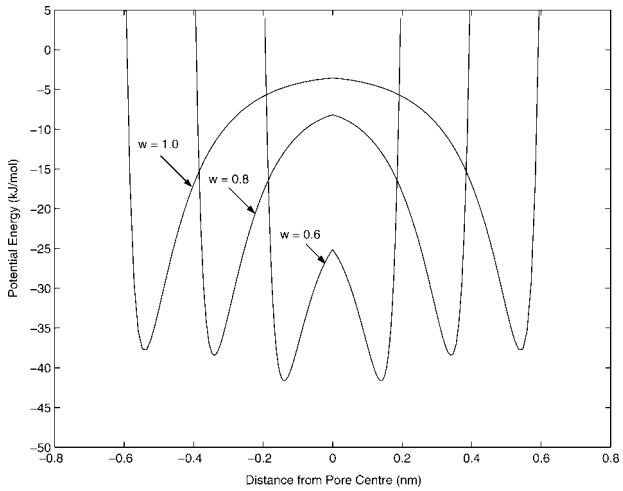

Figure 3. Potential energy profiles for CCl_4 in slit-shaped pores.

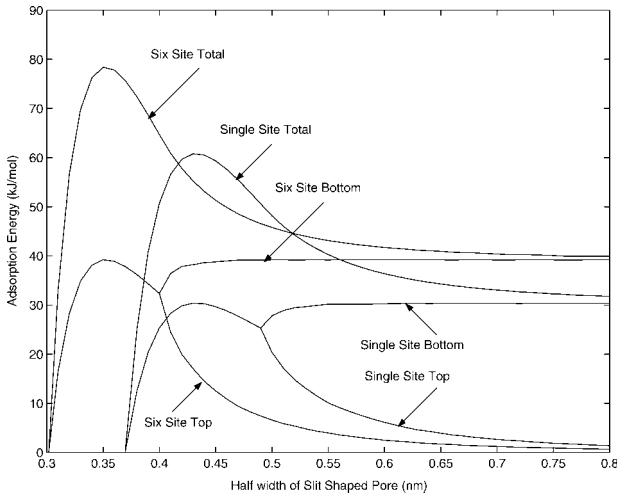

Figure 5. C_6H_6 adsorption energy profiles predicted by single- and six-site models.

The potential energy profiles for CCl_4 in a graphite slit pore with three different pore widths are depicted in Figure 3. It can be seen from Figure 3 that the smaller the pore size, the deeper the energy well. However, the difference between the energy well depths in the larger size range is less significant than that in the small-size range.

The three-dimensional (3-D) potential energy surface $\Phi(z, w)$ as a function of both pore size and location for CCl_4 in slit-shaped pores is shown in Figure 4. The detailed data of $\Phi(z, w)$ depicted in Figure 4 are used in numerical simulations together with the micropore-size distribution.

There are a number of potential models for benzene that have been proposed in the literature. A review of older models has been given by Vernov and Steele.[14] We use the model TraPPE proposed by Wick et al.[15] and further investigated by Do and Do[5] in this study. The model belongs to the general class of the united atom model. It has six dispersive sites, which coincide with the centers of six carbon atoms.

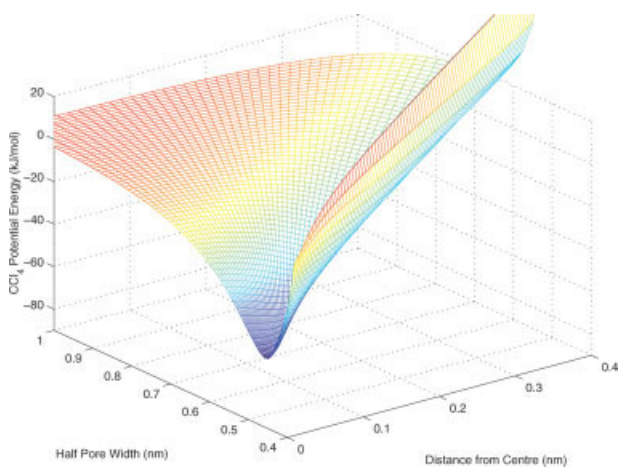

Figure 4. 3-D profile of CCl_4 potential energy in slit-shaped pore.

[Color figure can be viewed in the online issue, which is available at www.interscience.wiley.com.]

That is, a united site consists of a carbon and a hydrogen atom. The parameters of the model are: σ = 3.695 Å, ε/k_B = 50.0 K, and the C-C bond length is 1.4 Å, in which ε/k_B is the ratio between the characteristic energy and Boltzmann constant. Do and Do[5] have observed that at low-pressures, benzene molecules adopt the parallel orientation, and when the pressure is about 2,000 Pa, a small portion of benzene molecules change from parallel orientation to the slant or vertical orientation. This small portion can be estimated from their reported results using molecular dynamics simulations. Consequently, the computation of potential energies for the C_6H_6 system follows the same procedure as that for CCl_4 system described previously. The adsorption energy profiles of C_6H_6 for single-and six-site models are depicted in Figure 5. From Figure 5, it can be observed that in the pore-size range of w = 0.42–0.52 nm, the total adsorption energy computed by using the single-site model is higher than that computed based on multisite model. However, as $w > 0.52$ nm, this situation reverses. This trend is similar to the CCl_4 system. For both single and multisite models, there exists a pore-size range, in which the contributions from top and bottom are equal to each other. The 3-D potential energy surface $\Phi(z, w)$ as a function of both pore size and location for C_6H_6 in slit shaped pores is shown in Figure 6. Computations of potential energies as functions of both pore size and position are essential to the development of both oscillator and viscous models.

Oscillator Model

Model development

Two types of models, namely the oscillator model and the viscous model, have been developed by Jepps et al.[3] for the prediction of molecular transport in nanopores with uniform size. In this article, these are extended to more general systems with broad pore-size distributions. Ignoring fluid-fluid interactions, using the coordinate system (x, y, z) shown in Figure 1, the dynamics of a single molecule can be determined from the Hamiltonian given by

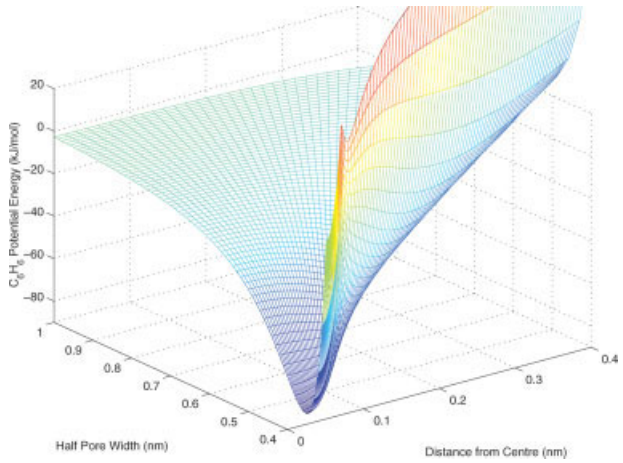

Figure 6. 3-D profile of C_6H_6 potential energy in slit-shaped pore.

[Color figure can be viewed in the online issue, which is available at www.interscience.wiley.com.]

$$H(z,w) = \Phi(z,w) - Fx + \frac{p_x^2}{2m} + \frac{p_y^2}{2m} + \frac{p_z^2}{2m} \tag{5}$$

where H is the Hamiltonian function, Φ the continuous potential accounting for solid-fluid interaction, F the magnitude of the external force field in the positive x direction, m the molecular mass, w the pore half-width, p_x, p_y and p_z are molecular momentums in three directions. The interactions between fluid molecules are referred to as "oscillations", and those between a fluid molecule and the pore wall as "reflections". Differentiation of Eq. 5 with respect to z gives

$$\frac{\partial H}{\partial z} = \frac{\partial \Phi}{\partial z} + \frac{p_z}{m}\frac{\partial p_z}{\partial z} \tag{6}$$

Since Hamiltonian function for each molecule is a constant, Eq. 6 leads to

$$E_z = \Phi(z,w) + \frac{p_z^2}{2m} \tag{7}$$

where E_z is the total energy in z-direction, which is a constant for a specified molecule. The energies in other two directions can be developed in a similar manner as follows

$$\begin{aligned} E_y &= \frac{p_y^2}{2m} \\ E_x &= -Fx + \frac{p_x^2}{2m} \end{aligned} \tag{8}$$

Molecular oscillations are confined in certain spaces. These restrictions can be determined by assessing the crossover points of the energy E_z, with the potential energy Φ, which are shown in Figure 7. From Figure 7, it can be shown that there are two types of crossover points between the E_z and Φ curves described as follows: as $E_z > \Phi(0, w)$, there are two crossover points, indicating that molecules oscillate between $-z_+$ and z_+, whereas as $E_z < \Phi(0, w)$, two pairs of crossover points form two spaces $\{-z_+, -z_-\}$ and, $\{z_-, z_+\}$ for molecular oscillation. These crossover points are computed for the determination of the period between successive collisions used in the computation of the diffusivity.

Extension of the oscillator model development by Jepps et al.[3] for molecular transport in nanopores with constant widths, provides the transport diffusivity $D_{\mu 0}$ for porous materials with broad pore-size distributions as

$$\begin{aligned} D_{\mu 0}(w) &= \frac{k_B T}{F}\langle v_x(w)\rangle \\ &= \frac{k_B T}{2m}\frac{\int_{-\infty}^{\infty}\int_{-w}^{w}\tau[E_z(z,p_z,w)]\exp[-E_z(z,p_z,w)/(k_B T)]dzdp_z}{\int_{-\infty}^{\infty}\int_{-w}^{w}\exp[-E_z(z,p_z,w)/(k_B T)]dzdp_z} \end{aligned} \tag{9}$$

where k_B is the Boltzmann constant, $\langle v_x\rangle$ is the average x velocity across the pore, and τ is the period between successive collisions. The method for the determination of τ proposed by Jepps et al.[3] is also extended to incorporate pore-size distributions

$$\begin{aligned} \tau(E_z,w) &= \sqrt{2m}\int_{-z_+(E_z)}^{z_+(E_z)}[E_z(z,p_z,w) - \Phi(z,w)]^{-1/2}dz \ \text{as} E_z > \Phi(0) \\ \tau(E_z,w) &= \sqrt{2m}\int_{z_-(E_z)}^{z_+(E_z)}[E_z(z,p_z,w) - \Phi(z,w)]^{-1/2}dz \ \text{as} E_z < \Phi(0) \end{aligned} \tag{10}$$

where z_+, z_- and $-z_+$ are defined in Figure 7. It is noteworthy that, since E_z, Φ and τ are all strong functions of pore size w, the simplified method based on averaged pore size leads to unacceptable errors for porous media with broad pore-size distributions, an observation previously made by the authors.[9] The recommended method for taking the size

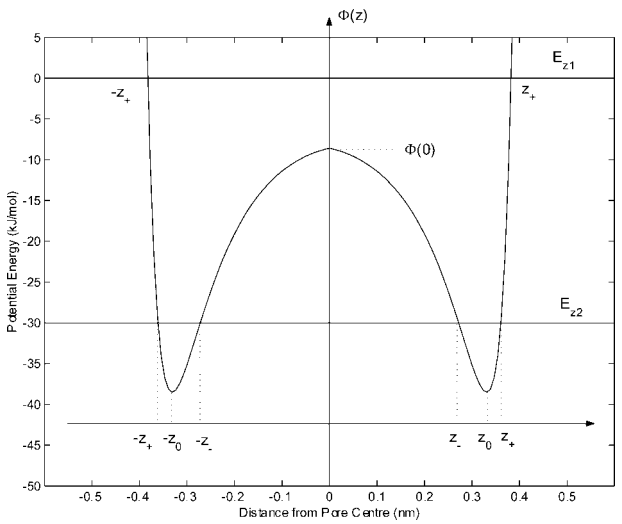

Figure 7. Range of molecular oscillation in slit-shaped pore.

distribution into account suggested by Wang et al.[9] for mass transfer through micropores in coal seams, is to replace the conventional diffusion equation given by

$$\frac{\partial C_\mu}{\partial t} = -\frac{\partial}{\partial z}(J_\mu) \qquad J_\mu = -D_\mu \nabla C_\mu \tag{11}$$

with

$$\frac{\partial \langle C_\mu \rangle_e}{\partial t} = -\frac{\partial}{\partial z}\langle J_\mu \rangle_e \qquad \langle J_\mu \rangle_e = -\langle D_\mu \nabla C_\mu \rangle_e \qquad \langle \bullet \rangle_e = \int_{w_{\min}}^{w_{\max}} \bullet f_d(\zeta) d\zeta \tag{12}$$

where $f_d(\zeta)$ is the dimensionless probability density function describing the pore-size distribution.

The average effective diffusivity $\langle D_\mu \rangle_e$ described by Eq. 13 is superior to that based on the averaged pore size $\langle w \rangle$ for the quick estimation of the diffusivity

$$\langle D_\mu \rangle_e = \int_{w_{\min}}^{w_{\max}} D_\mu(\zeta) f_d(\zeta) d\zeta \tag{13}$$

However, since the concentration of the adsorbed phase $C_\mu(w)$ is also a strong function of pore size w, which is not incorporated in $\langle D_\mu \rangle_e$, Eq. 12 should be used in dynamic simulations.[9]

Applicability of the oscillator model

It is well known that small particles, such as atoms and molecules, possess both particle and wave properties. However, the oscillator model is based on the classical theory, the applicability of which to molecular transport in nanopores can be tested by using the Heisenberg uncertainty principle as follows[16]

$$\Delta z \, \Delta p_z \geq \frac{\hbar}{2} \qquad \hbar = \frac{h}{2\pi} \tag{14}$$

where $h = 6.6256 \times 10^{-34}$ J-s, the Planck number. The uncertainty of the molecular velocity v is then estimated as

$$\Delta v \approx \frac{\hbar}{2m \, \Delta z} \tag{15}$$

Using molecular kinetics theory, the relative error is then

$$\frac{\Delta v}{v} = \frac{\hbar}{2\Delta z \sqrt{m k_B T}} \tag{16}$$

where T is the temperature. From Eq. 16, it can be seen that the smaller the pore size and the lighter the molecular weight, the larger the relative error. For example, if Δz is estimated as 2.5 Å, $\Delta v/v$ is about 2% for CH_4 molecules at 298 K. However, this value is increased to 6% for H_2 molecules under the same conditions. Consequently, models based on the classical theories should be used with caution for light molecules passing through narrow pores. For the CCl_4 and C_6H_6 transport in nanopores, because of the relatively large molecular weights (153.82 and 78.11, respectively), for the same position uncertainty Δz, $\Delta v/v$ is below 1%. This implies that if the pore size is not too close to the molecular size with a reasonable margin of Δz, the classical methods are satisfactory for CCl_4 and C_6H_6 transport in nanopores, without unacceptable errors. However, special attention must be paid to systems in which molecular size and pore width are very close to each other, since these cases may lead to significant errors due to very small Δz.

Viscous Model

Pure viscous model

In the development of the oscillator model, the fluid-fluid interactions are disregarded. This is only valid at low-densities. The viscous model of Jepps et al.[3] is applicable to a broad range of densities. From the Navier-Stokes relation and kinetic theory, Jepps et al.[3] provided the velocity in x-direction as

$$v_x(z) = \frac{F}{k\rho_0}\int_{-z_0}^{0} \rho(\xi) d\xi + \int_{-z_0}^{z} \frac{F}{\eta(\xi)} \int_{\zeta}^{0} \rho(\zeta) d\zeta d\xi \tag{17}$$

where F is the magnitude of external force acting on each molecule in the positive z-direction, ρ and η are density and viscosity, respectively, ρ_0 is the density at z_0, $\pm z_0$ as defined in Figure 7, and k is the friction coefficient described as

$$k = \sqrt{\frac{m k_B T}{2\pi}} \tag{18}$$

The transport diffusion coefficient, is, therefore, given by

$$D_\mu = \frac{k_B T}{2\,\widehat{\rho}\, F w}\int_{-z_0}^{z_0} \rho(z) v_x(z) dz = \frac{k_B T}{\widehat{\rho}\, w}\left[\frac{1}{k\rho_0}\left(\int_0^{z_0} \rho(\xi) d\xi\right)^2 + \int_0^{z_0} \frac{1}{\eta(z)}\left(\int_0^{z} \rho(\xi) d\xi\right)^2 dz\right] \tag{19}$$

The first and second terms in the righthand side of Eq. 19 account for the boundary reflections and effect of viscosity, respectively. The average density $\widehat{\rho}$ in Eq. 19 is defined as

$$\widehat{\rho} = \frac{1}{w}\int_0^w \rho(\zeta) d\zeta \tag{20}$$

The direct application of Eq. 19 to most porous materials of commercial interest is difficult for the following two reasons:

1. The diffusivity, density, and velocity are all strong functions of pore size represented as $D_\mu(w)$, $\rho(z, w)$ and $v_x(z, w)$. Given that a large number of important porous materials, such as coals and activated carbons, have broad pore-size distributions, new developments should reflect this reality.

2. The determination of molecule density profiles $\rho(z, w)$ requires molecular dynamic simulations using techniques, such as the equilibrium molecular dynamics (EMD), non-equilibrium molecular dynamics (NEMD), and grand canonical Monte-Carlo molecular dynamics (GCMD) as demonstrated by Bhatia and Nicholson.[1,2] A reliable and fast computational method for the determination of density profiles $\rho(z, w)$ as functions of both z and w has yet to be developed for industrial applications.

We seek a general and tractable method for molecular transport in nanopores with broad pore-size distributions. An acceptable approximation for the density profile under relatively low-pressures may be represented as

$$\rho(z,w) = \rho_\infty \exp\left[-\frac{\Phi(z,w)}{k_B T}\right] \tag{21}$$

where ρ_∞ is the density at the infinite temperature. The value of ρ_∞ is dependent on the pressure of bulk phase, but independent on the pore size. It can be computed by using Eq. 28, which will be explained later. Equation 21 is the standard Boltzmann solution for the canonical ensemble. It is a low-density solution in nanopores.[2] However, for weakly adsorbing materials, it could hold till reasonably high-pressures. Substituting Eq. 21 into Eq. 20 followed by the application of the integral mean value theory, gives

$$\hat{\rho}(w) = \rho_\infty \exp\left[-\frac{\Phi(w_m)}{k_B T}\right]; 0 \le w_m \le w \tag{22}$$

Similarly

$$\int_0^{z_0} \rho(z,w)dz = z_0 \rho_\infty \exp\left[-\frac{\Phi(z_{m0},w)}{k_B T}\right]; 0 \le z_{m0} \le z_0 \tag{23}$$

In Eqs. 22 and 23, w_m and z_{m0} are median points in integral mean value theory, which can be determined numerically. The boundary reflection term, denoted as $D_{\mu b}$ in Eq. 19, can be represented using the integral mean value as follows

$$\begin{aligned} D_{\mu b}(w) &= \frac{k_B T}{\widehat{\rho}\, w}\left[\frac{1}{k\rho_0}\left(\int_0^{z_0}\rho(\xi)d\xi\right)^2\right] \\ &= \frac{k_B T z_0^2}{kw}\exp\left[\frac{\Phi(w_m,w)+\Phi(z_0,w)-2\Phi(z_{m0},w)}{k_B T}\right] \\ &= \frac{k_B T z_0^2}{kw}\exp\left(-\frac{E_b}{k_B T}\right) \\ E_b &= |\Phi(w_m,w)+\Phi(z_0,w)-2\Phi(z_{m0},w)| \end{aligned} \tag{24}$$

It can be seen that Eq. 24 is structurally similar to a previously reported surface diffusivity model[7–9,17] given by

$$D_\mu(w) = D^0_{\mu,\infty}\exp\left[-\frac{aE(w)}{RT}\right] \tag{25}$$

In order to compute surface diffusivity using Eq. 25, it is necessary to estimate two unknown parameters, namely $D^0_{\mu,\infty}$ and a, using experimental measurements. In contrast, Eq. 24 developed in this article requires only the fundamental physical nature of the porous material, and does not require any curve fitting. Furthermore, it is apparent that the pre-exponential term in the surface diffusivity model should also be pore-size-dependent, a property which is not incorporated in the conventional computation of $D^0_{\mu,\infty}$.

The effect of viscosity is accounted for by the second term in the righthand side of Eq. 19 given by

$$\begin{aligned} D_{\mu v}(w) &= \frac{k_B T}{\widehat{\rho}\, w}\int_0^{z_0}\frac{1}{\eta(z,w)}\left(\int_0^z \rho(\xi,w)d\xi\right)^2 dz \\ &= \frac{k_B T \rho_\infty^2}{\widehat{\rho}\, w}\int_0^{z_0}\frac{1}{\eta(z,w)}\left(\int_0^z \exp\left[-\frac{\Phi(\xi,w)}{k_B T}\right]d\xi\right)^2 dz \end{aligned} \tag{26}$$

The density dependent viscosity η in Eq. 26 may be determined by a method developed by Chung et al.[18] Combining Eqs. 24 and 26 gives

$$\begin{aligned} D_\mu(w) &= D_{\mu b}(w) + D_{\mu v}(w) = \frac{k_B T}{w}\left[\frac{z_0^2}{k}\exp\left(-\frac{E_b}{k_B T}\right)\right. \\ &\left. + \frac{\rho_\infty^2}{\widehat{\rho}}\int_0^{z_0}\frac{1}{\eta(z,w)}\left(\int_0^z \exp\left[-\frac{\Phi(\xi,w)}{k_B T}\right]d\xi\right)^2 dz\right] \end{aligned} \tag{27}$$

In order to solve Eq. 27, the value of ρ_∞ must be determined. This can be done using the adsorbed phase concentration, which can be either experimentally measured or computed by using adequate adsorption isotherms. The mathematical expression for the adsorbed-phase concentration C_μ is

$$\begin{aligned} C_\mu(P) &= \int_{w_{\min}}^{w_{\max}} \hat{\rho}(w,P) f(w) dw \\ &= \int_{w_{\min}}^{w_{\max}} \frac{1}{w} f(w) \int_0^w \rho(z,w,P) dz dw \\ &= \rho_\infty(P) \int_{w_{\min}}^{w_{\max}} \frac{1}{w} f(w) \int_0^w \exp\left[-\frac{\Phi(z,w)}{k_B T}\right] dz dw \end{aligned} \tag{28}$$

Since the potential energy $\Phi(z, w)$, pore-size distribution $f(w)$, with the units of J/mol and m^3/(kg m), respectively, and the adsorption isotherm are all determined, $\rho_\infty(P)$ can be computed using Eq. 28. The techniques for the incorporation of size-dependent diffusivity given by Eq. 27 into the diffusion model with broad pore-size distribution are described by Eqs. 12 and 13.

It should be pointed out that Eq. 21 is only rigorous for low-pressure and density systems, which will lead to significant errors for high-pressure and density systems. The justification for the application of Eq. 21 in this work is explained as follows. First of all, we work on relatively low-pressures

Table 1. Physical Properties of Ajax Activated Carbon

Physical Properties	Numerical Value
Particle density ρ_P (kg/m^3)	733
Total porosity	0.71
Macro-pore porosity	0.31
Micro-/meso-pore porosity	0.40
Mean macro-pore radius (m)	8×10^{-7}
Macro-pore volume (m^3/kg)	4.7×10^{-4}
Micro-/meso-pore volume (m^3/kg)	4.4×10^{-4}
BET (N_2) surface area (m^2/kg)	1.2×10^{6}

and densities in this work, with the pressure well below 1 kPa (0.01 atm). Second, Eq. 21 is mainly used for the discovery of the physical insight of the widely used correlation described by Eq. 25, rather than for numerical computations. The boundary reflection contribution given by Eq. 24 will be replaced by the oscillator model represented by Eq. 9 in the hybrid model as explained later. The effect of the viscosity quantified by Eq. 26 only plays a minor role compared with the boundary reflection contribution, as will be demonstrated in the Results and Discussion section. Consequently, limitations of Eq. 21 will not lead to significant errors for the systems under current study.

It is important to note that the computation of the molar density using the adsorption isotherm requires the knowledge on pore-size distribution $f(w)$ in Eq. 28, which is normally measured based on the adsorption of the test gases, such as Ar, N_2 and CO_2. Since the test gases are different from the target gases under study, certain errors are introduced due to the connectivity and accessibility deviations between different gases. In the case studies carried out in this article, the connectivity and accessibility issues are collectively incorporated in the tortuosity function τ_μ (e.g., Eq. 34), which is adjusted using the measurement data. That is, the error from the identified sources can be minimized through parameter identification techniques in practice. Further work is needed to accurately quantify the connectivity and accessibility for different gases and their effects on adsorption isotherms.

Hybrid oscillator-viscous model

Based on molecular dynamics simulations, Jepps et al.[3] have realized that the oscillator model predicts the boundary reflection contribution better than that of the viscous model given by Eq. 24. Consequently, they proposed a hybrid modeling strategy for porous media with a uniform pore size. This strategy can be extended to the systems with broad pore-size distributions. Through the combination of Eqs. 9 and 26, the hybrid oscillation-viscous model is given by

$$D_\mu(w) = D_{\mu 0}^{OSC} + D_{\mu v}^{VIS} = \frac{k_B T}{2m} \frac{\int_{-\infty}^{\infty}\int_{-w}^{w} \tau[E_z(z,p_z,w)]\exp[-E_z(z,p_z,w)/(k_BT)]dzdp_z}{\int_{-\infty}^{\infty}\int_{-w}^{w} \exp[-E_z(z,p_z,w)/(k_BT)]dzdp_z} + \frac{k_B T \rho_\infty^2}{\widehat{\rho}\, w}\int_0^{z_0} \frac{1}{\eta(z,w)}\left(\int_0^z \exp\left[-\frac{\Phi(\xi,w)}{k_BT}\right]d\xi\right)^2 dz \quad (29)$$

As justified by Jepps et al.[3] the hybrid model performs better than the pure viscous model for systems with uniform nanopore size. It can be deduced that this observation is also valid for porous media with broad pore-size distributions. There are certain correlations between self-diffusivity[18] and surface diffusivity, which will be analyzed in the case study examples.

Carbon Tetrachloride and Benzene Transport in Activated Carbon

In this section, we apply the models developed in this work to CCl_4 and C_6H_6 transport in micro- and mesopores in an Ajax activated carbon. These systems have been experimentally studied by Bae and Do.[7,8]

Adsorption isotherms

It has been identified by Bae and Do[7,8] that the Toth isotherm equation is applicable to both systems, which is given as follows

$$C_\mu = C_{\mu s}\frac{bP}{\left[1+(bP)^t\right]^{1/t}} \quad (30)$$

The physical properties of the Ajax activated carbon reported by Bae and Do[7,8] are listed in Table 1. Using their original data, we have refitted the Toth parameters $C_{\mu s}$, b and t, for this work and report these below as "new", in Table 2, together with their "original" values as given by Bae and Do.[7,8]

The adsorption isotherm represented by Eq. 30 has been extended to systems with variable pore sizes by Wang and Do[17] as

$$C_\mu(w) = C_{\mu s}\frac{b(w)P}{\left[1+\left(b(w)P\right)^t\right]^{1/t}} \qquad b(w) = \frac{\beta}{\sqrt{MT}}\exp\left[\frac{E(w)}{RT}\right] \quad (31)$$

where the parameter β is assumed to be solid specific and independent with respect to adsorbate. We have applied this strategy in CO_2 and CH_4 adsorption on coals with reasonable results.[9] However, further study shows that the saturated adsorption concentration is a stronger function of pore size than the parameter b. Furthermore, it is more reasonable to use pore volume rather than adsorbent mass for the determination of adsorbate density. Consequently, the modified pore-size-dependent isotherm is defined as

Table 2. New and Original Toth Parameters for CCl_4 and C_6H_6 at 303 K

	CCl_4		C_6H_6	
Parameters	New	Original	New	Original
$C_{\mu s}$ (mol/g)	6.071×10^{-3}	7.194×10^{-3}	6.620×10^{-3}	6.301×10^{-3}
b (1/Pa)	0.7685	0.8447	0.7811	0.5055
t	0.3126	0.3653	0.3216	0.3213

$$\hat{\rho}(w) = \rho_s(w)\frac{b(w)P}{\left[1+\left(b(w)P\right)^t\right]^{1/t}} \tag{32}$$

where $\rho_s(w)$ is the saturated gas density and $\hat{\rho}(w)$ the averaged gas density defined by Eq. 20 in pores with half width of w. It must be pointed out that the Toth isotherm suggests a heterogeneous surface, which may not be consistent with the assumption that the local pore has the uniform pore size of w. However, when a small local zone is investigated, the variation of the pore size is normally restricted to a small value. Consequently, some mean values can be used for the local isotherms. That is, from the mathematical viewpoint, the notation "w" in Eq. 32 should be read as "in the vicinity of w". The determination of the parameters $\rho_s(w)$ and $b(w)$ together with their characteristics will be described in the Results and Discussion section.

The micro- and mesopore-size distributions for the Ajax activated carbon have been reported by Bae and Do,[8] and these are used in the simulations.

Permeability models

Since measured total permeability data are reported by Bae and Do,[8] we develop the permeability representations for different streams using the same permeability definition as these authors for easier comparison. The general definition of the permeability B is given by

$$J(P,w) = -B(P,w)\frac{\partial P}{\partial x} \tag{33}$$

This definition is different from the conventional definition of permeability K, although related through the relationship $B = K\eta$. The local surface flux j_μ in pores with the half width as w is represented as

$$\begin{aligned} j_\mu(w) &= -\frac{1}{\tau_\mu(P)}D_\mu(w)\frac{\partial\hat{\rho}(w)}{\partial x} \\ &= -\frac{1}{\tau_\mu(P)}D_\mu(w)\frac{\partial\hat{\rho}(w)}{\partial P}\frac{\partial P}{\partial x} \\ &= -\frac{1}{\tau_\mu(P)}D_\mu(w)\frac{\hat{\rho}(w)}{P}\left[1-\frac{(b(w)P)^t}{1+(b(w)P)^t}\right]\frac{\partial P}{\partial x} \end{aligned} \tag{34}$$

In Eq. 34, τ_μ is the micropore tortuosity, $\partial\hat{\rho}/\partial$P is computed using the Toth isotherm given by Eq. 32. Through an integration of Eq. 34 with the incorporation of pore-size distribution and solid density, the total surface flux J_μ and permeability B_μ in micropores are developed as follows

$$\begin{aligned} J_\mu &= -\frac{\rho_p}{\tau_\mu(P)}\left\{\int_{w_{\min}}^{w_{\max}} D_\mu(P,w)\frac{\hat{\rho}(P,w)}{P}\cdot\right. \\ &\quad \left.\times\left[1-\frac{(b(w)P)^t}{1+(b(w)P)^t}\right]f(w)\,dw\right\}\frac{\partial P}{\partial x} = -B_\mu\frac{\partial P}{\partial x} \\ B_\mu(P) &= \frac{\rho_p}{\tau_\mu(P)}\int_{w_{\min}}^{w_{\max}} D_\mu(P,w)\frac{\hat{\rho}(P,w)}{P}\left[1-\frac{(b(w)P)^t}{1+(b(w)P)^t}\right]f(w)\,dw \end{aligned} \tag{35}$$

where ρ_p is the particle density. The term $1-[(bP)^t/(1+(bP)^t]$ was omitted in the corresponding equations in the work reported by Bae and Do[8], (Eqs. 22 and 23 in Ref. 8), but this leads to significant errors in high-pressure regimes, which will be further analyzed in Results and Discussion section. Conventionally, an average diffusivity $\langle D_\mu\rangle_e$ defined by Eq. 13 is used for the mass-transfer computations. Eq. 35 can be simplified if the average diffusivity is used, as follows

$$B_{\mu C(P)} = \frac{\rho_p\langle D_\mu(P)\rangle_e}{\tau_\mu(P)}\int_{w_{\min}}^{w_{\max}}\frac{\hat{\rho}(P,w)}{P}\left[1-\frac{(b(w)P)^t}{1+(b(w)P)^t}\right]f(w)\,dw \tag{36}$$

However, we will also show in the Results and Discussion section that this simplification leads to unacceptable errors.

Knudsen diffusion takes place in mesopores. Incorporating pressure dependent tortuosity, the local molar flux j_K in pores with half width as w is described by the following equation

$$\begin{aligned} j_K(P,w) &= -\frac{1}{\tau_{me}(P)}D_K(P,w)\frac{\partial\hat{\rho}_{me}(P,w)}{\partial x} \\ &= -\frac{1}{\tau_{me}(P)}D_K(P,w)\frac{\partial\hat{\rho}_{me}(P,w)}{\partial P}\frac{\partial P(w)}{\partial x} \end{aligned} \tag{37}$$

where τ_{me} is the mesopore tortuosity, and the Knudsen diffusivity is given by

$$D_K(P,w)\big) = \frac{w}{2}\sqrt{\frac{8k_BT}{\pi m}}\left(\frac{2-f_P(P)}{f_P(P)}\right) \tag{38}$$

in which f_P is the reflection factor depending on the loading.[8] From Eq. 37 with the incorporation of the pore-size distribution and particle density, the total flux J_K and permeability B_K for Knudsen diffusion are given by

$$\begin{aligned} J_K &= -\frac{\rho_p}{\tau_{me}(P)}\left\{\int_{w_{me-}\min}^{w_{me-}\max} D_K(P,w)\frac{\partial\hat{\rho}_{me}(P,w)}{\partial P}f(w)\,dw\right\}\frac{\partial P}{\partial x} \\ &= -B_K\frac{\partial P}{\partial x} \\ B_K(P) &= \frac{\rho_p}{\tau_{me}(P)}\int_{w_{me-}\min}^{w_{me-}\max} D_K(P,w)\frac{\partial\hat{\rho}_{me}(P,w)}{\partial P}f(w)\,dw \end{aligned} \tag{39}$$

For solving Eq. 39, it is necessary to estimate the partial derivative $\partial\hat{\rho}_{me}/\partial$P. There are three ways to compute this derivative. The simplest method is to apply the gas law idea, leading to the relationship

$$\frac{\partial\hat{\rho}_{me}}{\partial P} = \frac{1}{RT} \tag{40}$$

The second method is to use an empirical correlation proposed by Bae and Do[8] to quantify the difference between the bulk and pore pressures as follows

$$P_{me} = P \exp\left(\frac{-\alpha E(w)}{RT}\right) \tag{41}$$

where P_{me} is the pressure within meso-pores and α is an empirical parameter to be determined experimentally. Equations 40 and 41 lead to

$$\frac{\partial \hat{\rho}_{me}}{\partial P} = \frac{\partial P_{me}}{\partial P_{me}} \frac{\partial \hat{\rho}_{me}}{\partial P} = \exp\left[\frac{-\alpha E(w)}{RT}\right] \frac{1}{RT} \tag{42}$$

The third method takes the molecule layering deduction into account, which is given by

$$P = \hat{\rho}_{me} \frac{V(w-\imath)}{V(w)} RT$$
$$\frac{\partial \hat{\rho}_{me}}{\partial P} = \frac{V(w)}{V(w-\imath)} \frac{1}{RT} \tag{43}$$

where V is the pore volume, and $\imath$ the thickness of molecule layering on the surface. The computational method for the determination of molecule layering thickness is developed by Bae and Do.[8] These three methods lead to the following final representation of the permeability contributed by the Knudsen diffusion

$$B_K(P) = \frac{\rho_p}{\tau_{me}(P) RT} \int_{w_{me-\min}}^{w_{me-\max}} D_K(P,w)\gamma(w) f(w)\, dw$$
$$\gamma(w) = 1 \quad \text{for Method 1}$$
$$\gamma(w) = \exp\left[\frac{-\alpha E(w)}{RT}\right] \quad \text{for Method 2}$$
$$\gamma(w) = \frac{V(w)}{V(w-\imath)} \quad \text{for Method 3} \tag{44}$$

All three methods are tested in our simulations with Method 3 as the recommended approach.

Estimation of tortuosity

The prime objective of this article is to develop diffusivity models for molecular transport in nanopores using basic material characteristics and reliable adsorption isotherms, rather than the characterization of porous materials. However, since the surface diffusivity is not directly measurable, the permeability measurements are used for the model validation, which depend on the material properties. In particular, the experimentally oriented models are used for the estimation of the tortuosity. This is not in conflict to our main conclusion that the newly developed models depend on neither molecular dynamics simulations nor curve fitting approaches. We now describe briefly the practical methods for the estimation of the tortuosity for the model validation using the literature data.

The first method was described in Mohanty et al.[20] as follows

$$\frac{\varepsilon}{\tau} = 1.522 \frac{(z_c - 1)^3}{(z_c - 1)^2} (\varepsilon - \varepsilon_c)^2 \tag{45}$$

where ε is the porosity, the coordination number z_c, and the percolation threshold ε_c are given by Dullien[21] as

$$(1-\varepsilon) = 1.072 - 0.1193 z_c + 0.004312 {z_c}^2$$
$$\varepsilon_c = \frac{1}{z_c - 1} \tag{46}$$

A single pore type was assumed in the original developments.[20,21] There are three pore types in the activated carbon, namely, macro-, meso- and micropores. The normal application is to combine micropores with solids, and define the total porosity as the summation of the macro- and mesopores given by[9]

$$\varepsilon = \varepsilon_{ma} + (1 - \varepsilon_{ma})\varepsilon_{me} \tag{47}$$

where $\varepsilon_{ma,}$ and ε_{me} are macroporosity and mesoporosity, respectively. Using Eqs. 45–47, and the porosity data of the Ajax activated carbon listed in Table 1, the tortuosity for the combined macro-/mesopores is computed as: $\tau = 2.9$, which is lower than that estimated by Do and Do[22] and Bae and Do[8] as $\tau = 4.0$–6.0. In this work, we modify Eq. 45 as follows to fit the reported data for mesopores

$$\frac{\varepsilon_{me}}{\tau_{me}} = 1.522(1 - \varepsilon_{ma}) \frac{(z_c - 1)^3}{(z_c - 1)^2} (\varepsilon_{me} - \varepsilon_c)^2 \tag{48}$$

The estimated values are as follows $\tau_{me} = 4.2$; $z_c = 6.3$; and $\varepsilon_c = 0.19$, which are all close to the literature data.

The second method is the application of the Archie's law to estimate the tortuosity of mesospores explained by Sahimi[23] as follows

$$\frac{\varepsilon_{me}}{\tau_{me}} = \varepsilon_{me}^{v} \tag{49}$$

where v is the parameter to be determined experimentally. The range of v estimated by Sahimi[23] is from 1.3 to 4. In this work, $v = 2.2$ leads to the same values as estimated using the first method.

The applicability of these two methods to micropores with very small pore sizes remains as an unanswered question. However, both correlations can be used for qualitative analysis. For example, the tortuosity is very sensitive to the coordination number z_c as shown by Eq. 48. As z_c decreases from 6.3 to 4.6, the tortuosity increases from 4.2 to 134.3. This observation will be used for the explanation of the variations of the pressure dependent, micropore tortuosity in the Results and Discussion section. In this work, the adjustment of the tortuosity in micropores using the measurement data is only carried out for one system (CCl_4-adsorbent). The successful application of the similar tortuosity-pressure relationship to another system (C_6H_6) justifies the validity of this relationship.

Results and Discussion

Molecular density distribution

An accurate determination of the molecular density is necessary for solving the viscous model described by Eqs. 24, 26 and 27. In all simulations, we fix the temperature at $T = 303.16$ K (30°C). For the fixed temperature, the molecular density function $\rho(w, z, P)$ consists of three independent vari-

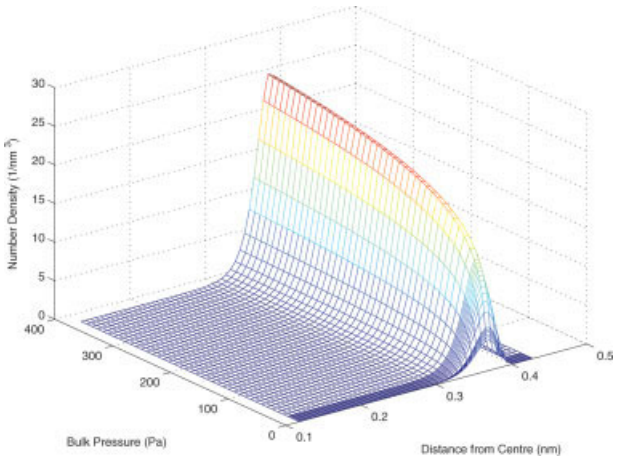

Figure 8. CCl_4 molecular density with fixed pore size (w = 0.71 nm).

[Color figure can be viewed in the online issue, which is available at www.interscience.wiley.com.]

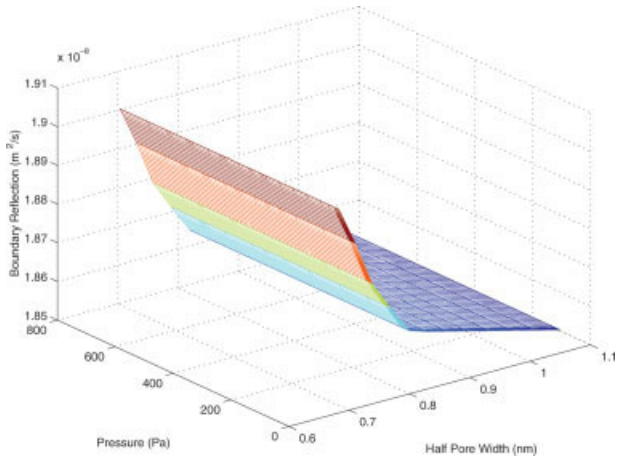

Figure 10. Boundary reflection contribution to diffusivity of CCl_4 (T = 303 K).

[Color figure can be viewed in the online issue, which is available at www.interscience.wiley.com.]

ables, namely pore size, molecular location and bulk pressure, requiring rendition in four-dimensions. As illustrations, we present a couple of 3-D diagrams to show the major characteristics of molecular density distributions. Figure 8 shows a 3-D CCl_4 molecular density surface as a function of bulk pressure and molecular location with fixed pore size (w = 7.1 Å). The diagram indicates that molecular densities increase with the bulk pressure, with the peaks corresponding to the locations of the energy wells as shown in Figures 3 and 4. Similar diagrams can be obtained for other pore sizes.

The 3-D diagram of ρ-w-z surface for CCl_4 is presented in Figure 9. The figure shows that in the small pore-size regime, the smaller the pore size, the higher the density peak until a nearly identical profile is formed for larger pores. This is because the adsorption energies increase sharply with the decrease of pore sizes for smaller micropores, but approach a constant for larger micropores with the numerical value close to the adsorption energy on a single plate.

Similar trends are obtained for C_6H_6 density configurations with different numerical values, which are omitted in this article.

Surface diffusion in nanopores

We use the hybrid oscillator-viscous model given by Eq. 29 to compute the surface diffusivity, in which the oscillator and viscous models are described by Eqs. 9 and 26, respectively. The oscillator model is not an explicit function of the molecular density. Its contribution to the surface diffusivity decreases monotonically with pore size increase, as shown in Figure 10. The 3-D diagram $D_{\mu v}$-P-w is shown in Figure 11, illustrating the effect of viscosity on diffusivity of CCl_4. The viscosity effect on the diffusivity increases with pressure, which is consistent with the results reported by Jepps et al.[3] However, in contrast to the sharp diffusivity drop with increasing pore size in the smaller pore-size regime, the sur-

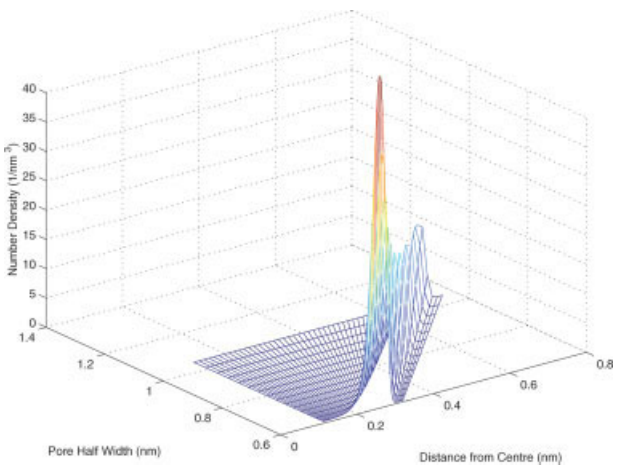

Figure 9. CCl_4 molecular density with fixed pressure (P = 245.7 Pa, T = 303 K).

[Color figure can be viewed in the online issue, which is available at www.interscience.wiley.com.]

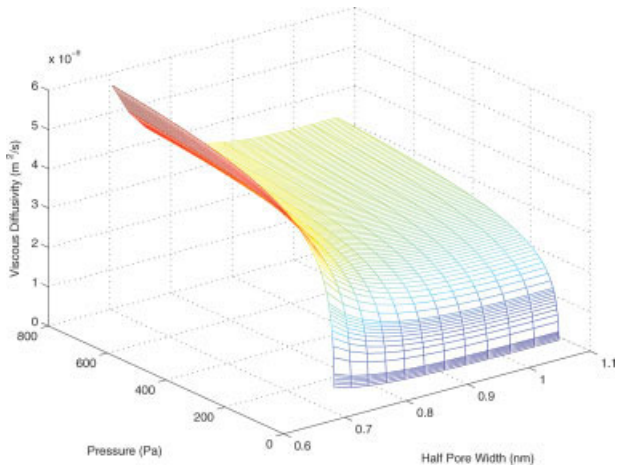

Figure 11. Viscosity contribution to diffusivity of CCl_4 (T = 303 K).

[Color figure can be viewed in the online issue, which is available at www.interscience.wiley.com.]

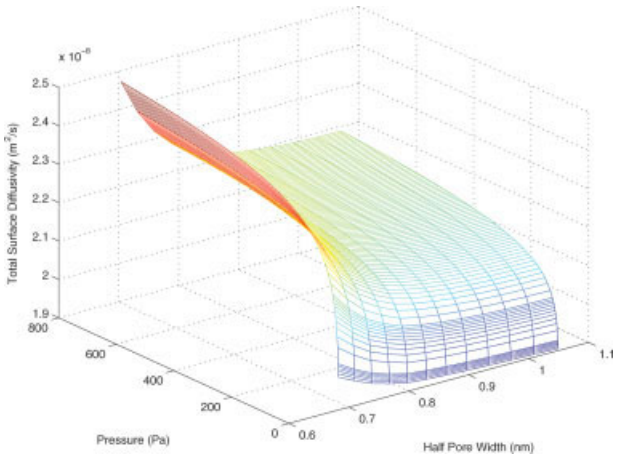

Figure 12. Total surface diffusivity of CCl_4 (T = 303 K).

[Color figure can be viewed in the online issue, which is available at www.interscience.wiley.com.]

face depicted in Figure 11 is not very sensitive to pore size in the larger pore-size regime. This is due to much stronger adsorbent-adsorbate interactions in smaller pores than in larger ones.

The total surface diffusivity of CCl_4 in micropores computed using Eq. 29 is depicted in Figure 12. The trends and magnitude are consistent with that reported by Jepps et al.[3] However, since they worked on methane, which has a much smaller molecular weight and size than CCl_4, our data are lower in approximately the ratio of (D_{μ_CH4}/D_{μ_CCl4}) estimated from the ratio of self-diffusivity (D_{s_CH4}/D_{s_CCl4}). The self-diffusivity at normal pressures can be roughly estimated using the correlation proposed by Mathur and Thodos[18] as follows

$$(PD_s)\delta = 44.0 \times 10^{-5} {T_r}^{1.716} \quad \text{for } T_r > 1.5$$
$$(PD_s)\delta = 2.427 \times 10^{-5}(7.907T_r - 1.66)^{1.638} \quad \text{for } T_r < 1.5$$
$$\delta = M^{1/2} {T_c}^{5/6} {P_c}^{2/3} \tag{50}$$

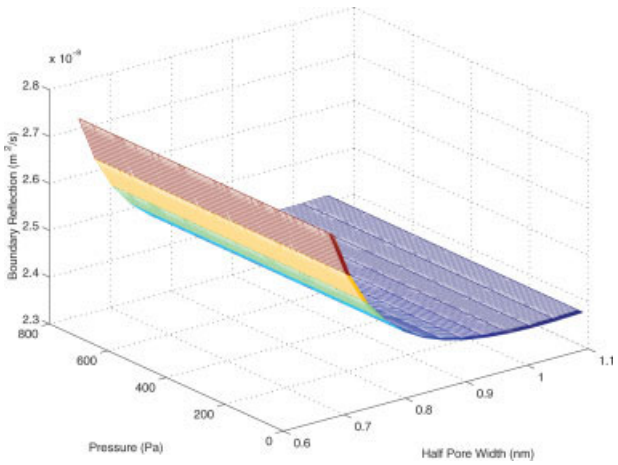

Figure 13. Boundary reflection contribution to diffusivity of C_6H_6 (T = 303 K).

[Color figure can be viewed in the online issue, which is available at www.interscience.wiley.com.]

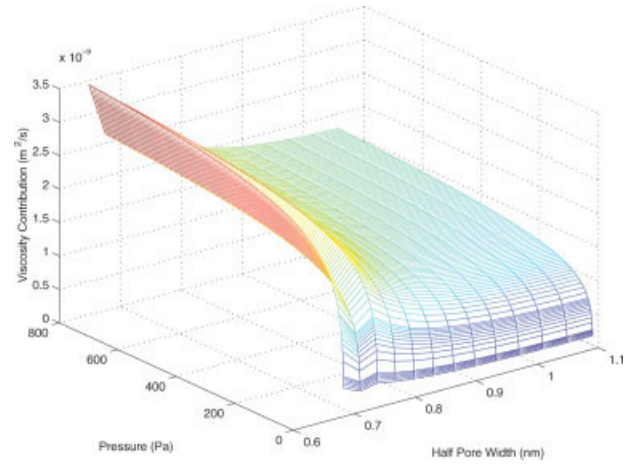

Figure 14. Viscosity contribution to diffusivity of C_6H_6 (T = 303 K).

[Color figure can be viewed in the online issue, which is available at www.interscience.wiley.com.]

where the subscripts c and r stand for "critical" and "reduced", respectively, and the unit of pressure P is atm.

Similar diagrams of the boundary reflection and viscosity contributions to the diffusivity, as well as total surface diffusivity are shown in Figures 13–15, respectively. We note from simulations that the self-diffusivities for both CCl_4 and C_6H_6 computed using Eq. 50 overestimate the surface diffusivities at the pressures under investigation. However, the ratio between self-diffusivities of CCl_4 and C_6H_6 is close to that between surface diffusivities of both species.

From Figures 10−15, one can observe that although the viscosity contribution to the total surface diffusivity is not negligible, it plays a relatively minor role compared with the effect from boundary reflections. When the hybrid model is applied, the effect of boundary reflections is quantified by the oscillator model, which does not rely on Eq. 21 for the determination of molecule densities. Consequently, the limitations of Eq. 21 do not lead to unacceptable errors in our case studies.

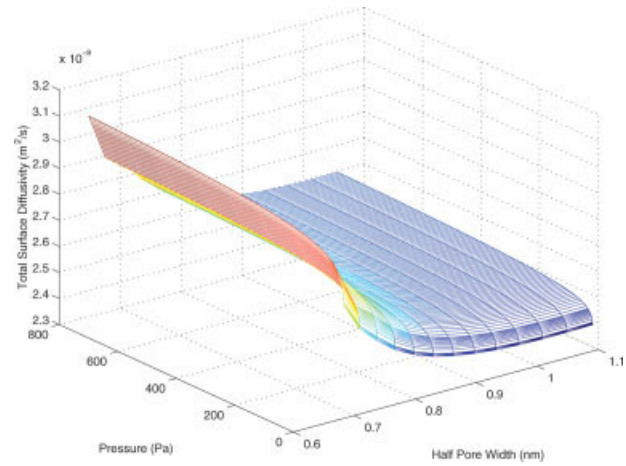

Figure 15. Total surface diffusivity of C_6H_6 (= 303 K).

[Color figure can be viewed in the online issue, which is available at www.interscience.wiley.com.]

Pore-size-dependent local isotherms

The conventional pore-size-dependent isotherm proposed by Wang and Do[17] represented by Eq. 31, assumed a variable parameter $b(w)$, but a constant saturated concentration $C_{\mu s}$. The improved isotherm model described by Eq. 32 proposed in this work assumes both parameter $b(w)$, as well as the saturated density $\rho_s(w)$, are functions of pore size w. Since the local densities can be computed using the model developed in this work, local isotherm representations can be justified. Using the simulated data for, $\hat{\rho}(P,w)$, the saturated molecular number density ρ_s, and parameter b can be estimated. For CCl_4 adsorption, it can be shown that $b(w)$ varies from 0.76 – 0.89 Pa^{-1}, but ρ_s decreases from 6.6 to 0.8 nm^{-3}, with the increase of w, as depicted in Figure 16. Consequently, the improved local isotherm represented by Eq. 32 provides better predictions of the adsorption behavior than the conventional one. Another important variable is the partial derivative of the local isotherm with respect to pressure. The following equation can be developed through partial differentiation and algebraic operations

$$\frac{\partial\hat{\rho}(P,w)}{\partial P}=\frac{\hat{\rho}(P,w)}{P}f_c$$
$$f_c=1-\frac{\left(b(w)P\right)^t}{\left[1+\left(b(w)P\right)^t\right]} \tag{51}$$

The factor f_c is omitted in the model developed by Bae and Do,[8] which is only accurate as $P\rightarrow 0$. The relationships between f_c and P are depicted in Figure 17 for CCl_4 and C_6H_6, which shows that the higher the pressure, the smaller the factor f_c. The omission of f_c requires an adjustment of other parameters to fit the experimental data.

Permeability issues

The simulation results for B_μ, $B_{\mu c}$, B_K and $B_t = B_\mu + B_K$ using current models, together with the experimentally measured B_t reported by Bae and Do[8] for CCl_4 are depicted in Figure 18, with good agreement between model prediction and experimental data. Importantly, although the trends of

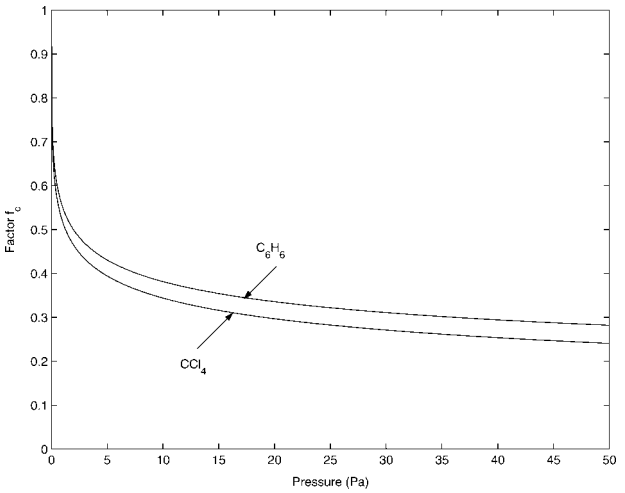

Figure 17. Relationship between factor f_c and pressure.

B_μ, B_K and B_t profiles shown in Figure 18 are very similar to that reported by Bae and Do,[8] different physical insights are revealed. Rectifying the omission of the function represented by $f_c = 1-[(bP)^t/(1+(bP)^t]$, as in Bae and Do models[8] for the computations of surface diffusion coefficient and flux, requires also that the other model parameters are adjusted to correctly predict B_μ. It transpires that the missing function is compensated by the variations of tortuosity in micropores. Under low-pressures, the tortuosity in micropores is very high due to low-connectivity. The connectivity increases with pore pressure, because of adsorption induced edge-plain swelling reported by Ustinov and Do[24] and Wang et al.,[9] and the removal of loose fines driven by pressure, which attach the originally disconnected channels. The tortuosity of micropores approaches a constant at certain pressure, when essentially all connections are engaged. The micropore permeability starts to reduce after this switching pressure. From Figure 18, it can be shown that this switching point is around $C_\mu =$

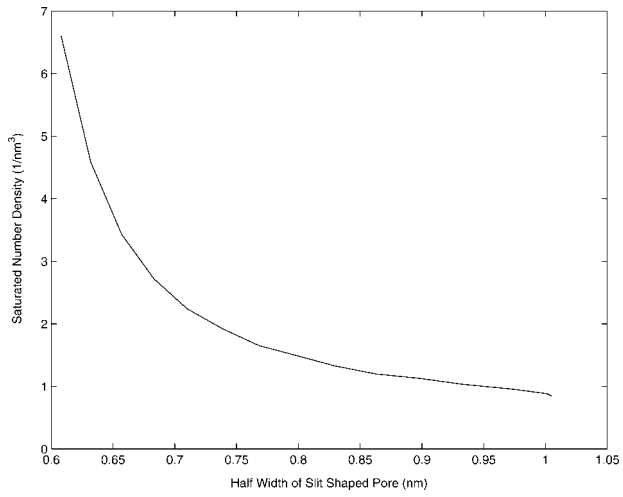

Figure 16. Relationship between saturated molecular density and pore size.

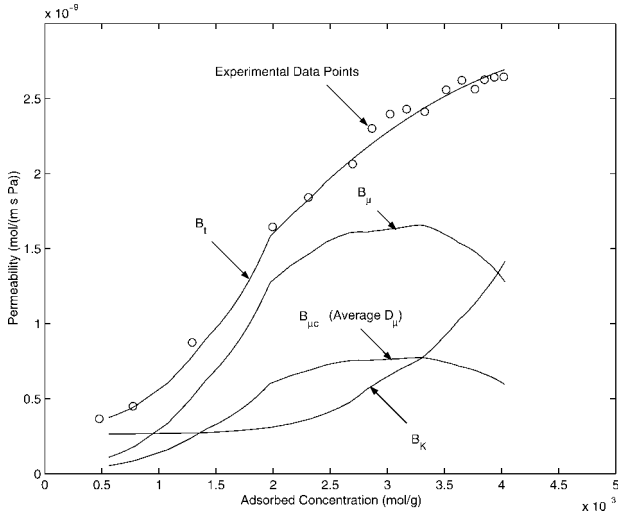

Figure 18. Permeability of CCl_4 in micro-/mesopores of ajax activated carbon.

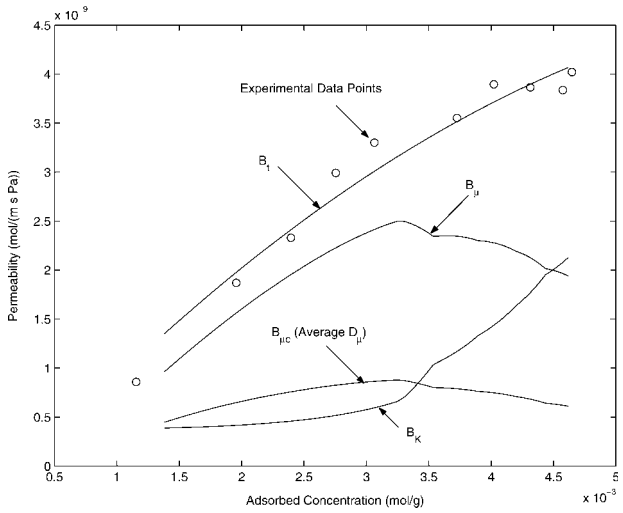

Figure 19. Permeability of C_6H_6 in micro-/mesopores of ajax activated carbon.

0.003 mol/g (P = 150 Pa) for the CCl_4 system. The tortuosity variations with coordination number/connectivity can be quantified by Eq. 45. It can be shown that 20% decrease of z_c leads to a reduction of tortuosity from 150 to 20, which is the range of the tortuosity variations observed in simulations.

Simulations are also carried out to determine various permeability values for C_6H_6-activated carbon with similarly good agreement with experimental data. B_μ, $B_{\mu c}$, B_K and B_t profiles, together with experimental data are shown in Figure 19. One of the most important reasons to choose two case study systems is that the tortuosity as a function of pressure is not directly measurable. However, if the tortuosity estimated for one system is applicable to another system using the same adsorbent, it can be considered that the estimated tortuosity is reliable. This target is achieved since the tortuosity-pressure relationships for both CCl_4 and C_6H_6 systems are very similar.

Another important point observed from Figures 18 and 19 is that the computations of the permeability using the distributed diffusivity $D_\mu(P, w)$, and averaged diffusivity $\langle D_\mu \rangle_e$ represented by Eqs. 35 and 36, respectively, lead to very different results. The relative error could be up to 40% for CCl_4 as shown in Figure 18. This error is much more severe for the C_6H_6 system as demonstrated by Figure 19. Consequently, the average values of the pore-size-dependent parameters in micropore models should not be used in simulations. They should only be used for gaining a general sense of the order of the parameters.

Conclusions

Models of the molecular transport in micro-/mesopores with broad pore-size distributions are developed in this article. The simulation results compared to experimental outcomes reported in the literature lead to the following conclusions.

1. The modeling approach developed in this work provides a solution requiring only elementary structural characteristics of the porous material and a reliable adsorption isotherm, eliminating empirical extraction of key parameters[7–9,17] or cumbersome molecular dynamics simulations.[1–3,10] It extends the method proposed by Jepps et al.[3] by eliminating three major limitation of their original work, namely (1) uniform pore size, (2) molecules assumed as regular hard spheres, and (3) of the need to use molecular dynamics simulations for the determination of density distributions. Simulation results for two case study systems, namely CCl_4 and C_6H_6 transport in an Ajax activated carbon show good agreement with the reported data.

2. The multisite potential energy models for the quantification of fluid-fluid and fluid-solid potentials developed by Do and Do[4,5] allows the application of well-known Lennard-Jones 12-6, and Steele 10-4-3 equation to large molecule systems. Single-site potential models lead to significant numerical errors for both CCl_4-carbon and C_6H_6-carbon interaction potentials.

3. The strategy of using parameters averaged over pore sizes, conventionally used in micropore models, is shown to lead to significant errors in both case study systems, as also pointed out previously by the authors in a study on mass transfer in coal seams.[9] For micropore simulations, pore-size-dependent parameters should be used, as described in this work. However, it could be acceptable to apply effectively averaged parameters in meso- and macropore models.[9]

4. The application of the integral mean value theory to the viscous model shown in Eq. 24 provides a physical basis for the empirical model for the surface diffusivity[7–9,17] described by Eq. 25. While the empirical model (Eq. 25) requires two empirical parameters, the fundamental form (Eq. 24) requires only physical information about the porous medium.

5. Surface diffusivity profiles are theoretically obtained in this article for an Ajax activated carbon characterized by Bae and Do,[7,8] showing good agreement with the experimental measurements. The importance of the tortuosity and connectivity variation is illuminated through an analysis of the simulation data, drawing on recent advances in adsorption induced pore swelling.[9,20] The increase of the surface diffusion induced permeability with the rise of pressure in the low-pressure regime can be attributed mainly to the higher connectivity from micropore swelling and removal of pore obstacles under pressure. The higher connectivity leads to significant reduction in tortuosity. This analysis is justified by similar tortuosity-pressure relationships obtained for two case study systems.

6. The saturated molecular density ρ_s in the local isotherm models with pore-size-dependent characteristics should also be a function of pore size. The pore size effect on ρ_s is much more significant than that on other isotherm parameters b and t as demonstrated in the case studies.

Notation

a = ratio of activation energy to adsorption energy, dimensionless
B = permeability, mol/(m s Pa)
b = parameter in Toth isotherm equation, 1/Pa
C_μ = adsorbed concentration, mol/m^3
D = diffusivity, m^2/s
E = adsorption energy, J/mol
E_z = total energy of a molecule in z-direction, J/molecule
F = magnitude of external force field acting on a molecule, N/molecule

f = pore-size distribution, m/(kg m)
f_c = factor developed from partial differentiation of local isotherm, dimensionless
f_d = probability density function describing pore-size distribution, dimensionless
f_p = loading dependent reflection factor, dimensionless
H = Hamiltonian function, J/molecule
h = Plank constant, 6.6218×10^{-34} J s
$\hbar$ = h/2π, 1.05459×10^{-34} J s
J = molar flux, mol/(m^2 s)
$j(w)$ = local molar flux as a function of pore size, mol/(m^2 s)
k = friction coefficient, kg m/s
k_B = Boltzmann constant, 1.38066×10^{-23} J/K
k_{sf} = solid-fluid binary interaction parameter, dimensionless
L = distance between two atoms, m or Å
M = molecular weight, based on carbob-12 as 12.00000
m = molecular mass, kg/molecule
n_c = number of sites in a molecule, dimensionless
P = pressure, N/m^2 or Pa
p = molecular momentums, kg m/s
R = gas constant, 8.31441 J/(K mol)
T = temperature, K
t = parameter in Toth isotherm equation, dimensionless
V = pore volume, m^3
v = molecular velocity, m/s
w = half width of slit-shaped pores, m
z_c = coordination number of pore network, dimensionless
z_i = distance between the atom i of the fluid molecule and the central plane of the pore, m
$[-z_+ \; z_+]$ = range of molecular oscillation Case 1
$[z_- \; z_+]$ = range of molecular oscillation Case 2

Greek letters

α = empirical parameter in Eq. 41, dimensionless
β = adsorbent specific parameter, 1/Pa
β = property of solid, m^3/mol (g K mol^{-1})$^{1/2}$
γ = parameter defined in Eq. 44 accounting for nonideality, dimensionless
Δ = spacing of lattice layers, m
ϵ = characteristic energy, J
ε = potential well depth, J/mol
ε = particle porosity, dimensionless
ε_c = percolation threshold, dimensionless
η = viscosity, N s/m^2
ι = thickness of molecular layer on pore surface, m
ν = parameter in the Archie's law, dimensionless
ρ = gas density in pores, mol/m^3 or 1/nm^3
ρ_p = particle density, kg/m^3
ρ_s = number of lattice atoms per unit volume, 1/m^3
σ = collision diameter, m
τ = period between successive collisions, s
τ_{me} = tortuosity of meso-pores, dimensionless
τ_μ = tortuosity of micro-pores, dimensionless
Φ = potential energy, J/mol

Literature Cited

1. Bhatia SK, Nicholson D. Hydrodynamic origin of diffusion in nanopores. *Phys Rev Letts*. 2003;90:016105-1–016105-4.
2. Bhatia SK, Nicholson D. Molecule transport in nanopores. *J Chem Phys*. 2003;119:1719–1730.
3. Jepps OG, Bhatia SK. Modeling molecule transport in slit pores. *J Chem Phys*. 2004;120:5396–5406.
4. Do DD, Do HD. Adsorption of carbon tetrachloride on graphitized carbon black and in slit graphitic pores: Five-site versus one-site potential models. *J Phys Chem B*. 2006;110:9520–9528.
5. Do DD, Do HD. Adsorption of benzene on graphitized carbon black: Reduction of the quadrupole moment in the adsorbed phase. *Langmuir*. 2006;22:1121–1128.
6. Do DD. *Adsorption Analysis: Equilibria and Kinetics*. London: Imperial College Press; 1998.
7. Bae J-S, Do DD. Surface diffusion of strongly adsorbing vapors in activated carbon by a differential permeation method. *Chem Eng Sci*. 2003;58:4403–4415.
8. Bae J-S, Do DD. Permeability of subcritical hydrocarbons in activated carbon. *AIChE J*. 2005;51:487–501.
9. Wang FY, Zhu ZH, Massarotto P, Rudolph V. Mass transfer in coal seams for CO_2 sequestration. *AIChE J*. 2007;53:1028–1049.
10. Bhatia SK, Jepps OG, Nicholson D. Tractable molecular theory of transport of Lennard-Jones fluids in nanopores. *J Chem Phys*. 2004;120:4472–4485.
11. Reid RC, Prausnits JM, Poling BE. *Properties of Gases and Liquids*. 4th ed. New York: GcGraw-Hill; 1987.
12. Steele WA. *The Interaction of Gases with Solid Surface*. Oxford: Pergamon; 1974.
13. Rao MB, Jenkins RG, Steele WA. Potential functions for diffusion in carbon molecular sieves. *Langmuir*. 1985;1:137–141.
14. Vernov A, Steele WA. Computer simulations of benzene adsorbed on graphite, 1 & 2. *Langmuir*. 1991;7:2817–2820 & 3110–3117.
15. Wick CD, Martin MG, Siepmann JIJ. Transferable potentials for phase equilibrium. 4. United-atom description of linear and branched alkenes and alkyl-benzenes. *Phys Chem B*. 2000;104:8008–8016.
16. Richtmyer FK, Kennard EH, Cooper JN. *Introduction to Modern Physics*. 6th ed. New York: McGraw-Hill; 1969.
17. Wang K, Do DD. Multicomponent adsorption, desorption and displacement kinetics of hydrocarbon on activated carbon - dual diffusion and finite kinetic model. *Sep Purif Technol*. 1999;17:131–146.
18. Chung T-H, Ajlan M, Lee LL, Starling KE. Generalized multiparameter correlation for nonpolar and polar fluid transport properties. *Ind Eng Chem Res*. 1988;27:671–679.
19. Mathur GP, Thodos G. The self-diffusivity of substances in the gaseous and liquid states. *AIChE J*. 1965;11:613–616.
20. Mohanty KK, Ottino JM, Davis HT. Reaction and transport in disordered composite media: Introduction of percolation concepts. *Chem Eng Sci*. 1982;37:905–942.
21. Dullien FAL. *Porous media: Fluid transport and pore structure*. San Diego: Academic Press; 1992.
22. Do DD, Do HD. Non-isothermal effects on adsorption kinetics of hydrocarbon mixture in activated carbon. *Sep Purif Technol*. 2000; 20:49–65.
23. Sahimi M. *Flow and transport in porous media and fractured rock: From classical methods to modern approaches*. Weinheim: VCH; 1995.
24. Ustinov EA, Do DD. Effect of adsorption deformation on thermodynamic characteristics of a fluid in slit pores at sub-critical conditions. *Carbon*. 2006;44:2652–2663.

Manuscript received Nov. 24, 2007, and revision received Apr. 15, 2008.